Journal of Materials Chemistry A

PAPER

View Article Online
View Journal | View Issue

Cite this: J. Mater. Chem. A, 2019, 7, 513

Insights into Li/Ni ordering and surface reconstruction during synthesis of Ni-rich layered oxides†

Yandong Duan,‡[ab] Luyi Yang,‡[a] Ming-Jian Zhang,[ab] Zonghai Chen,[c] Jianming Bai,[d] Khalil Amine,[c] Feng Pan*[a] and Feng Wang*[b]

Received 2nd November 2018
Accepted 3rd December 2018

DOI: 10.1039/c8ta10553g

rsc.li/materials-a

Nickel-rich layered transition metal oxides (NMCs) have been intensively studied as promising cathode candidates for next-generation Li-ion batteries, known for low cost and high theoretical capacity. However, the practical capacity of NMCs is largely determined by cationic ordering and has yet to be well controlled during synthesis, largely due to the complexity and *non-equilibrium* nature of the reactions occurring in the sintering process. In this work, high-energy synchrotron X-ray diffraction is employed to investigate the kinetic and thermodynamic aspects of cationic ordering during synthesis of $LiNi_{0.7}Mn_{0.15}Co_{0.15}O_2$ (NMC71515). It is found that cationic ordering in the bulk is coupled to surface reconstruction during synthesis, occurring concomitantly and both being greatly affected by Li_2CO_3 decomposition and Li loss at the particle surface. Through tuning the sintering temperature and time, highly ordered NMC71515 with high capacity and excellent rate capability is synthesized. The developed approach may be applied broadly to the synthesis of high-performance Ni-rich NMC and other cathode materials.

Introduction

Lithium-ion batteries (LIBs) are considered as one of the most attractive power sources for electrical energy storage in modern civilization, especially in the field of electric vehicles.[1–3] However, the growing demands for energy storage devices with high energy density and long cycling life require significant improvements in currently used LIBs. In the past three decades, many types of electrode materials have been proposed and studied, such as layered lithium transition metal oxides,[4–6] spinel lithium transition metal oxide,[7] and polyanion compounds.[8] Among them, layered lithium transition metal oxides ($LiNi_{1-x-y}Mn_xCo_yO_2$, NMC) are the most promising due to their high energy densities and tailorable properties by atomic substitution.[9] To date, Ni-rich NMC materials ($LiNi_{1-x-y}Mn_xCo_yO_2$, $x + y \leq 0.3$) have been intensively studied for higher energy density cathode candidates, which offer capacity over 220 mA h g^{-1} at cutoff voltages above 4.5 V. However, there are still challenges to be overcome for the practical use of NMC materials in commercial LIBs. One of the major problems is Li/Ni anti-sites. According to our recent work,[10] in layered NMC materials, the spin interactions of transition metal (TM) ions construct a triangular network with geometrical frustration, which will inevitably lead to lattice instability. The formation of Li/Ni anti-sites in MNC will not only relieve the degeneracy of the frustrated magnetic lattice, but also introduce a 180° superexchange interaction, which further relieves the magnetic frustration through the emergence of new exchange paths. In recent years, enormous efforts have been devoted to reducing Li/Ni anti-sites.[11–17] However, these understanding are all based on the thermodynamic view. The control of cationic ordering during the real synthesis process from the kinetic view is still a great challenge.

High-energy X-ray diffraction (HEXRD) has proven to be a powerful tool capable of tracking synthesis reactions in preparing battery materials under real synthesis conditions.[18–22] In our previous study, *in situ* HEXRD analysis of $LiNi_{0.8}Co_{0.2}O_2$ revealed that the degree of cationic ordering first rises then falls with the temperature.[23] In a subsequent study, time-resolved *in situ* HEXRD and X-ray absorption spectroscopy (XAS) were combined to track the kinetics of both cationic ordering/disordering and grain growth during heat treatment of $LiNi_{0.7}Mn_{0.15}Co_{0.15}O_2$ (NMC71515).[24] Recently, a multimodal synchrotron X-ray studies, including XRD, PDF and XAS, on the structural evolution during the *in situ* synthesis of

[a]School of Advanced Materials, Peking University, Shenzhen Graduate School, Shenzhen 518055, People's Republic of China. E-mail: panfeng@pkusz.edu.cn

[b]Sustainable Energy Technologies Department, Brookhaven National Laboratory, Upton, New York 11973, USA. E-mail: fwang@bnl.gov

[c]Electrochemical Technology Program, Chemical Sciences and Engineering Division, Argonne National Laboratory, Argonne, Illinois 60439, USA

[d]National Synchrotron Light Source II, Brookhaven National Laboratory, Upton, NY, 11973, USA

† Electronic supplementary information (ESI) available. See DOI: 10.1039/c8ta10553g

‡ These authors contributed equally to this work.

$LiNi_{0.7}Mn_{0.15}Co_{0.15}O_2$ further revealed that, the symmetry reconstruction of NiO_6 octahedra due to O gaining is the synthetic origin of cationic ordering above 500 °C.[25] All these works indicate that temperature is the key factor affecting the kinetics of cationic ordering in Ni-rich NMC material. Nevertheless, more systematic studies are needed to gain insight into how the cationic ordering can be tuned.

Surface reconstruction significantly affects the chemical composition as well as the electrochemical performance of many battery materials, especially layered oxides.[26–28] Layered oxides tend to react with atmospheric CO_2 to form Li_2CO_3 residue at the particle surface, which can lead to gas evolution[29,30] and significantly affect the electrochemical performance.[27,31] Therefore, the balance between Li_2CO_3 formation and decomposition at the surface can be viewed as an important surface reconstruction process for NMC materials. In addition, Li/O loss from the particle surface at high temperature has been observed during the sintering process.[32–34] This is another type of surface reconstruction that has significant impact on material synthesis. Since the surface chemistry of layered oxides is sensitive to the synthesis conditions, such as ambient gas and sintering temperature, it is of great importance to investigate the synthetic tuning of NMC materials by taking account of surface reconstruction reactions. However, the intrinsic correlation between surface reconstruction and cationic ordering still remains unclear.

Based on the above discussion, the most urgent task to obtain structurally ordered NMC material is to establish a universal correlation between the synthesis conditions and the structural evolution. Herein, we systematically explored the kinetic and thermodynamic properties of cationic ordering/disordering during the preparation of NMC71515 by HEXRD, under various synthesis conditions (*i.e.* temperature and time). It has been revealed that cationic ordering of NMC71515 is highly correlated to surface reconstruction reactions *via* Li_2CO_3 decomposition and Li/O loss during synthesis. Consequently, by controlling the synthesis conditions within the ideal range, NMC71515 with high cationic ordering can be obtained by balancing Li_2CO_3 decomposition and Li/O loss, which delivered the optimized electrochemical performances.

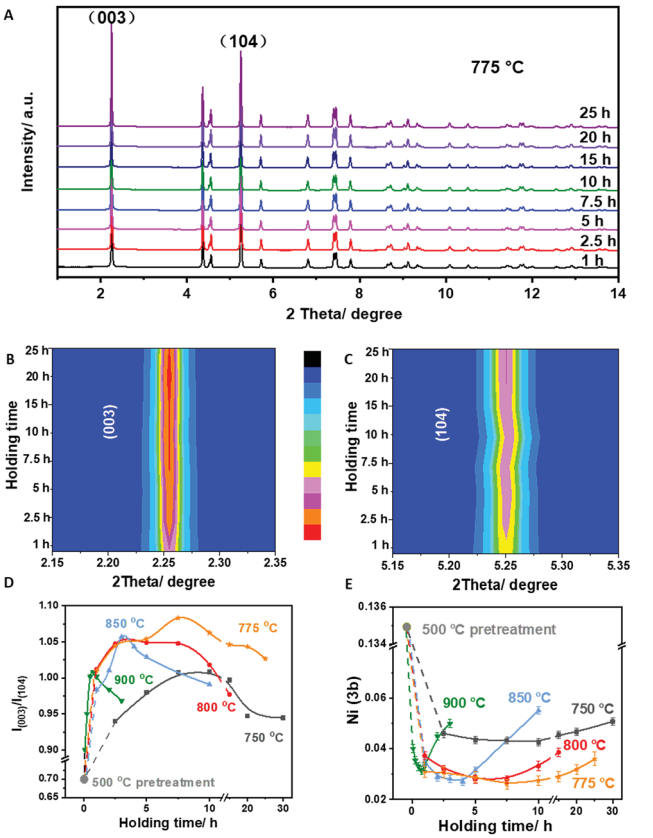

Fig. 1 Dependence of cationic ordering in NMC71515 on sintering temperature and holding time. (A) Synchrotron X-ray diffraction (XRD) patterns from NMC71515 sintered at 775 °C (see also Fig. S2 to S5† for data from samples sintered at other different temperatures). (B and C) XRD contour plots in the selected angle regions containing (003) and (104) peaks, respectively. (D) Intensity ratio of peak (003) to (104) (denoted as $I_{(003)}/I_{(104)}$) as a function of holding time for samples sintered at different temperatures. (E) Occupancy of Ni at 3b sites (*i.e.*, Li sites), Ni(3b), as a function of holding time for samples sintered at different temperatures.

Results and discussion

Cationic ordering control

The full XRD pattern of NMC71515 pre-heated at 500 °C is presented in Fig. S1,† where a very low content of Li_2CO_3 is evident. The formation of Li_2CO_3 is mainly due to the reaction between CO_2 in the atmosphere and LiOH in the raw materials during preparation. *Ex situ* HEXRD patterns of NMC71515 at 775 °C for different sintering times are shown in Fig. 1A. Other results obtained at 750 to 900 °C are presented in Fig. S2–S5.† The contour maps for the (003) and (104) peaks are extracted in Fig. 1B and C, respectively. As a result, for all sintering temperatures, the curves for the changes of the intensity ratio of (003) to (104) (I_{003}/I_{104}) show n-shaped trends where this ratio first increases with holding time then decreases (shown in Fig. 1D). Since the I_{003}/I_{104} ratio is positively correlated to the degree of Li/Ni ordering in NMC materials,[35] it is expected that cationic ordering increases then decreases with time. To obtain additional details about structural evolution, Rietveld refinements have been made to all XRD patterns (detailed data are presented in Tables S1–S6†). Fig. 1E shows the changes in the occupancy of Ni at 3b sites in Li layers (Ni(3b)) with sintering time at different sintering temperatures. The curves indicate that the change of Ni(3b) shows a u-shaped trend, where it first decreases with holding time to a minimum value then increases. Because a lower value of Ni(3b) indicates a more ordered structure, the curves in Fig. 1E are in good agreement with the I_{003}/I_{104} trend. In addition, the ratio of lattice parameters, c/a, also demonstrates the degree of ordering in the layered structure. In Fig. S6,† the c/a values show very similar variations over holding time and temperature to those of I_{003}/I_{104}. The bond lengths for Li–O, TM–O, and Li slabs (presented in Fig. S7†) exhibit similar trends.

The above results reveal that, for each sintering temperature, there is an optimized sintering time (t_o) at which the highest

degree of cationic ordering with minimum Li/Ni anti-sites is obtained. At 775 °C, t_o is found to be 7.5 hours, which is greatly shortened to 45 minutes as the sintering temperature increases to 900 °C. Here, the processes of structural ordering and disordering can be considered as forward and reverse reactions, both of which can be expedited by increasing the sintering temperature. As demonstrated in Fig. 2A, at the beginning of sintering, the increasing degree of order is ascribed to the forward reaction rate (ν_f) being higher than that of the reverse reaction rate (ν_r) due to its lower activation energy.[36] As the reaction proceeds, ν_r gradually increases until $\nu_f = \nu_r$ (at t_o). At this point, an equilibrium state is reached where structures with the highest degree of order have the minimum Li/Ni anti-sites.

Since elevated temperature generally leads to higher reaction rate coefficients, a shorter t_o can be also expected. After reaching t_o, the overall reaction rate ($\nu_f - \nu_r$) becomes negative, leading to a disordering process with increasing Li/Ni anti-sites. Furthermore, Fig. 1D and E demonstrate that the minimum Li/Ni anti-site values at t_o also differ with sintering temperature: at t_o samples sintered at 775, 800, and 850 °C show a similar number of Li/Ni anti-sites, whereas the samples sintered at 750 and 900 °C have much higher degree of cationic disordering. Fig. 2B and C show how Ni(3b) changes with sintering time during cationic ordering and disordering, respectively. First, for the ordering process, all data points in Fig. 2B can be fit with the equation:

$$y = A\exp(-k_1x) + c_1 \quad (1)$$

where A is the pre-exponential factor, k_1 is the reaction rate constant of the ordering process, and c_1 is a constant. The Arrhenius plot of reaction rate k_1 is presented in Fig. 2D. It exhibits good linearity from 775 to 900 °C. As a result, the activation energy (E_a) is estimated to be 189 kJ mol^{-1} by fitting the linear slope according to the equation:

$$\ln(k) = \ln(A) - E_a/RT \quad (2)$$

where R is the gas constant, and T is the absolute temperature. In contrast, the data point for 750 °C is off the linear fit, suggesting a different E_a as well as a different reaction mechanism. Different from the ordering process, the data points in Fig. 2C can be fit with the linear equation:

$$y = k_2x + c_2 \quad (3)$$

where k_2 is the reaction rate constant of the disordering process, and c_2 is a constant. Similarly, as shown in Fig. 2E, the E_a of the disordering process was calculated to be 194 kJ mol^{-1} based on eqn (2). In this case, the data point at 900 °C deviates from the linear fit. Therefore, it is of great importance to further explore the origins of the irregularities in kinetic behaviour at these two temperatures.

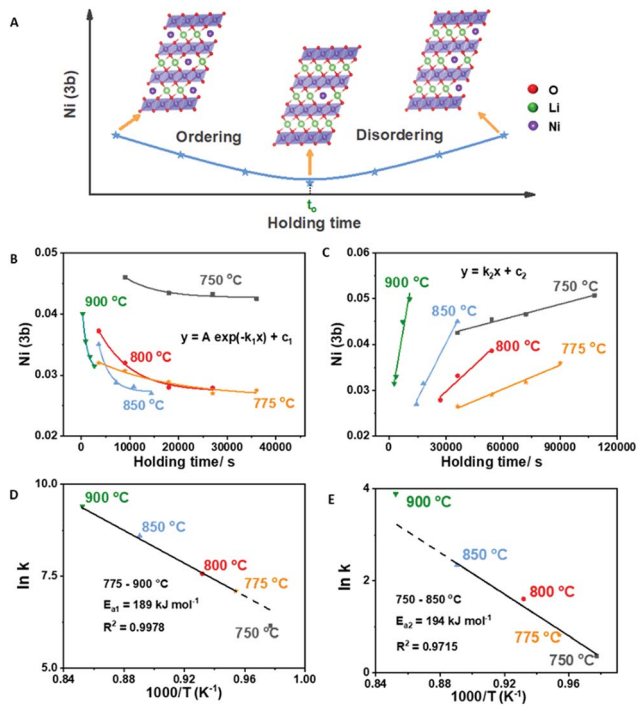

Fig. 2 Kinetic aspects of cationic ordering in NMC71515. (A) Schematic illustration of cationic ordering and disordering processes. (B) Change of Ni(3b) in NMC71515 with holding time during ordering process. Solid lines are the fitting results based on an exponential equation. (C) Change of Ni(3b) in NMC71515 with holding time during disordering process. Solid lines are linear fitting results. (D and E) Arrhenius plots of the kinetic constants determined for the cationic ordering and disordering processes, respectively.

Surface reconstruction

We performed structural/chemical analyses for both the bulk and surface of the NMC71515. From the XRD patterns (Fig. 3A–E and S8†) and X-ray photoelectron spectra (XPS) (Fig. 3F; detail data are presented in Table S7, and Fig. S9†) of NMC71515 sintered at different temperatures, it can be seen that the sample sintered at 750 °C contains a much higher content of Li_2CO_3 compared to other samples, which is also confirmed by the elemental mapping in Fig. S10.† Fig. 3F shows a large discrepancy of Li_2CO_3 content between 750 and 775 °C, whereas no obvious Li_2CO_3 consumption can be seen from 500 °C (preheated sample) to 750 °C. The thermogravimetric analysis (TGA) for Li_2CO_3 in Fig. S10† also indicates that after reaching the decomposition temperature (733 °C), the decomposition rate for the sample held at 750 °C is much lower compared with rates for other temperatures. Previously, it had been reported that the reaction between atmospheric CO_2 and the raw material forming Li_2CO_3 on the particle surfaces is reversible at the critical temperature, where the forward reaction is kinetically favourable.[37] Therefore, before the decomposition temperature of Li_2CO_3 is reached (*i.e.*, 733 °C), there is no extra driving force to consume Li_2CO_3. Although 750 °C is above the decomposition temperature of Li_2CO_3, its consumption rate is still relatively low compared with its formation rate, which leads to an unchanged overall content of Li_2CO_3 on NMC71515 particle surfaces. By contrast, at 775 °C, the decomposition rate of Li_2CO_3 is high enough to exceed its formation rate. It is notable that after the Li_2CO_3 sample reached 40.5% of initial weight, which indicates the complete decomposition of Li_2CO_3 into Li_2O, the weight continues decreasing very gradually owing to

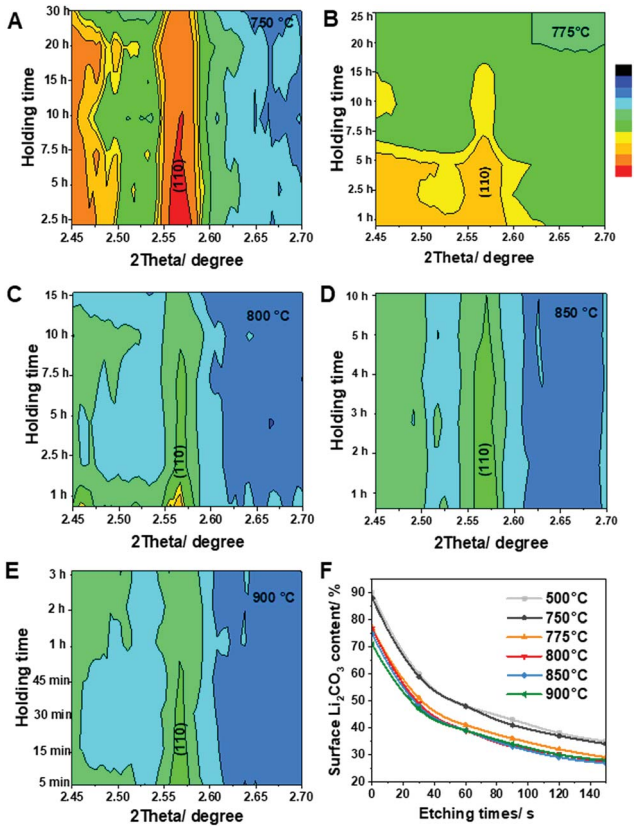

Fig. 3 Formation of Li_2CO_3 with holding time at different temperatures. (A–E) Contour plots of the XRD patterns in the selected 2θ regions containing Li_2CO_3 (110) peak at sintering temperatures from 750 °C to 900 °C. (F) Li_2CO_3 contents measured from XPS for different etching time (estimated from the ratio of peak areas for $O_{Li_2CO_3}$: O_{total}).

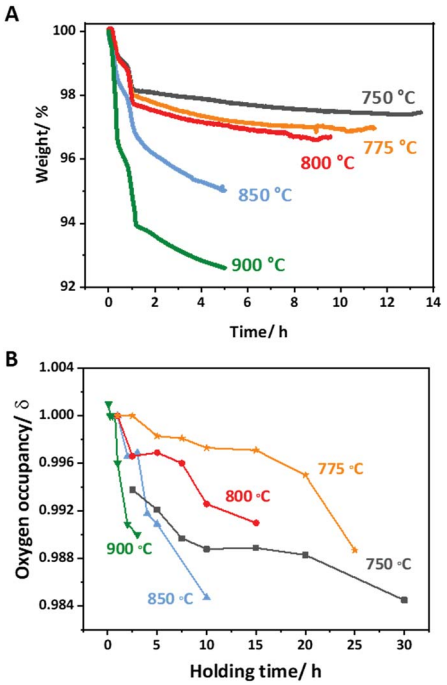

Fig. 4 Lithium and oxygen loss in NMC71515 during sintering. (A) Weight loss of NMC71515 during holding at different temperatures, measured by TGA. The samples were heated at a rate of 5 K s^{-1}. (B) Oxygen occupancy (O_{6C}) as a function of holding time at different temperatures.

Li/O loss at high temperature (Fig. S11†). The surface reconstruction on NMC71515 particles for Li_2CO_3 during cationic ordering is proposed to follow the reactions below:[24]

$$Li_2CO_3 \rightarrow Li_2O + CO_2 \quad (4)$$

$$m(Li_{1-x}Ni_x)_{3b}(Ni_{0.7-0.3x-0.7z}Mn_{0.15+0.15x-0.15z}Co_{0.15+0.15x-0.15z}Li_z)_{3a}O_2 + nLi_2O + n/2O_2 \leftrightarrow (Li_{1-y}Ni_y)_{3b}(Ni_{0.7-0.3y-0.7v}Mn_{0.15+0.15y-0.15}Co_{0.15+0.15y-0.15v}Li_v)_{3a}O_2 \quad (5)$$

where $m = (1 + y)/(1 + x)$ and $n = (x - y)/(1 + x)$ for $x > y$. Therefore, the unreacted Li_2CO_3 residue on the NMC71515 particle surface not only brings about electrochemically inactive Li ions, but also acts as a passivation layer, which barricades Li ion diffusion from the particle surface into the bulk. As a result, the surface construction of NMC71515 particles is inhibited by Li_2CO_3 under insufficient temperature, which leads to Li-deficient phases. The different state for Li-ion diffusion at 750 °C also explains its abnormal kinetic behaviour in Fig. 2D.

To probe the cause of higher cationic disordering at t_o when calcination is done at 900 °C, we performed TGA measurements of pre-heated NMC71515 at different temperatures. The results are presented in Fig. 4A, where continuous weight loss can be observed for NMC71515 with sintering time. In addition, the weight loss increases with higher sintering temperature, especially at 900 °C. Since the stabilized weights in Fig. 4A vary with sintering temperatures, this weight loss should not be due to Li_2CO_3 decomposition. Instead, as stated previously, the weight loss can be mainly attributed to the Li/O loss during heating. The oxygen occupancy (O_{6C}) results in Fig. 4B from XRD refinement suggest that the oxygen occupancy monotonically decreases with sintering time. The Li/O loss mainly happens at the surface due to the broken symmetry at the surface of crystallites. This results in a Li/O-deficient phase at the particle surface, which gradually spreads into the bulk during the phase balancing process. ICP measurement was carried out to analyse the element composition of NMC71515 sintered at 900 °C, 45 min and 900 °C, 5 h. As shown in Table S8,† the weight loss of the elements is consistent with TGA results. At 900 °C, the oxygen occupancy plunges with sintering time, indicating that an accelerated Li/O loss process generates different disordering kinetics. This finding explains the great deviation at 900 °C in the Arrhenius plot shown in Fig. 2E. This phenomenon not only partially accounts for the cationic disordering beyond t_o, but also suggests that at an elevated temperature (*i.e.*, 900 °C or higher), the surface reconstruction owing to Li/O loss is too fast to actually reach a thermodynamically stable state. In brief, surface Li/O loss can induce Li-ion diffusion from the bulk to the surface, leaving more Li vacancies for Li/Ni anti-sites and a less Ni-ordered structure at t_o.

Based on the above, we concluded that surface reactions have significant impacts on the cationic ordering/disordering

kinetics in the bulk. On the one hand, insufficient sintering temperatures (as shown in Scheme 1A) do not provide enough driving force for Li_2CO_3 decomposition as well as Li-ion diffusion during the ordering process, leading to Li-deficient structures with more Li/Ni anti-sites. Therefore, by increasing the sintering temperature to a suitable range of 775 to 850 °C (shown in Scheme 1B), the decomposition of Li_2CO_3 enables a cationic ordered structure in the bulk. However, as shown in Scheme 1C, when the temperature is too high (*e.g.* 900 °C), although the temperature is high enough for the structural ordering process, the rate of Li/O loss is also greatly accelerated. This phenomenon finally leads to Li-deficient phase near the particle surface, which then gradually propagates to the bulk over time.

Once Li vacancies in Li-layers are created, Ni atoms in adjacent TM layers tend to migrate towards Li layers as Ni(3b), resulting in less ordered structures with numerous Li/Ni anti-sites. Thus, by sintering NMC71515 within the temperature range between 775 °C and 850 °C, desirable surface reconstruction (decomposition of Li_2CO_3) is fast while unwanted surface degradation (Li/O loss) is relatively slow, resulting in a higher degree of Li/Ni ordering. At the temperature of 775 °C, optimized ordering/disordering kinetics can be obtained within a time frame of approximately 5 hours, which is error tolerant and beneficial to the synthesis.

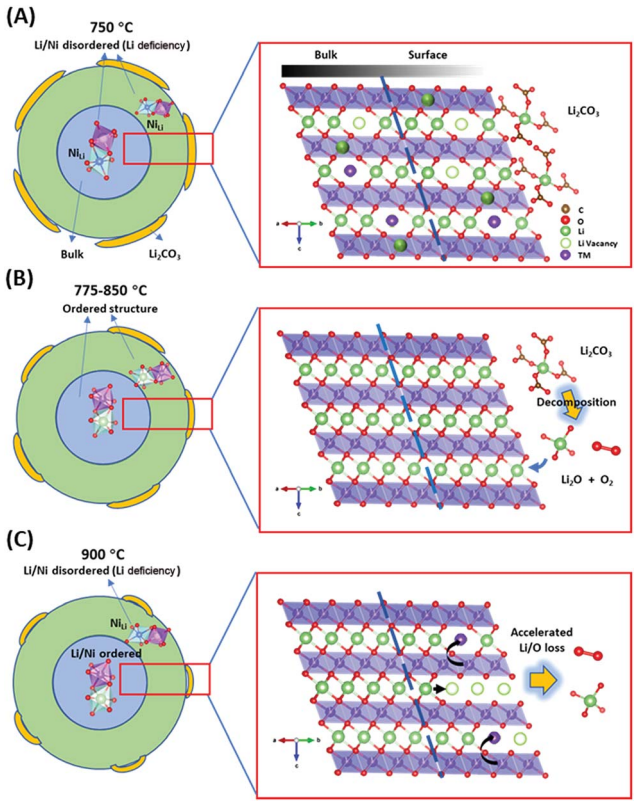

Scheme 1 Schematic illustrations of how cationic ordering is coupled to surface reconstruction of NMC71515 under different sintering temperatures: (A) when the temperature is too low, unreacted Li_2CO_3 leads to Li-deficient phase in the bulk; (B) under ideal sintering condition, a Li/Ni ordered structure can be achieved due to the decomposition of Li_2CO_3; (C) when the temperature is too high, Li/O loss from the surface brings about Li-deficient phase.

Electrochemical performance

To obtain the correlation between electrochemical performance and sintering conditions of NMC71515, we carried out galvanostatic cycling experiments for materials prepared with sintering time of t_o at different temperatures. Fig. 5A shows that the sample sintered at 775 °C attained the highest capacity (189 mA h g^{-1}), followed by samples sintered at 850 °C (187 mA h g^{-1}), 800 °C (183 mA h g^{-1}), and 900 °C (180 mA h g^{-1}). In contrast, the sample sintered at 750 °C attained the lowest first-cycle capacity (156 mA h g^{-1}) and the lowest discharge voltage. This result agrees with the degree of cationic ordering for each sample. In more ordered structures, there will be more electrochemically active Li sites, hence, the higher capacities. The larger amount of Li_2CO_3 residue on the surface of the sample sintered at 750 °C could also lead to lower capacity.

The rate performance of the different cells is compared in Fig. 5B. It can be clearly observed that, at C rates of 0.1C, 0.2C, 0.5C, 1C, 2C, and 5C, superior rate performance is demonstrated by the samples sintered at 750 °C and 775 °C. followed by the samples sintered at 800 °C and 850 °C, whereas the sample sintered at 900 °C delivers the poorest rate capability.

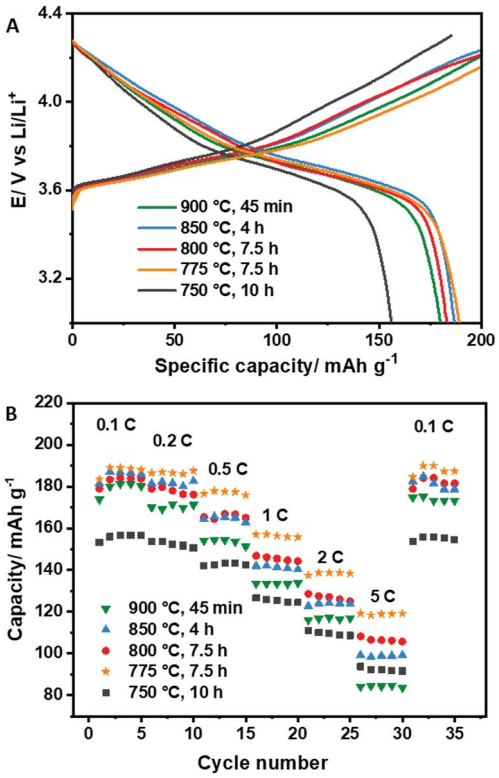

Fig. 5 Electrochemical performance of NMC71515 sintered at different temperatures. (A) Galvanostatic charge/discharge profiles and (B) rate performances of NMC 71515 sintered for optimized time (t_o) at different temperatures (1C = 200 mA g^{-1}). The areal loading of active material is approximately 0.8 mg cm^{-2}.

The different sizes of NMC71515 crystallite prepared under different sintering temperature were estimated from scanning electron microscope (SEM) and XRD measurements, and the results (Fig. S12 and Table S9†) indicate that the crystallite size increases with sintering temperature. Therefore, one can speculate that the rate performance is highly correlated with the grain size since the reduced particle size will not only decrease the diffusion distance for Li ions, but also increase the specific surface area (as shown in Fig. S13†), leading to more efficient and faster charge transport and ion diffusion.[38] Note that although the sample sintered at 750 °C has smaller crystallite size, the unreacted Li_2CO_3 has limited its rate capability, therefore it is out performed by the sample sintered at 775 °C. In addition, it can be seen that when the capacity is reverted back to 0.1C, good capacity retention (*e.g.* 99.6% for sample sintered at 775 °C) can be obtained. Since the capacity of NMC material is largely dependent on its cationic ordering, this is a strong evidence of well retained cationic ordering after Li-ion insertion and extraction. In order to further investigate the electrochemical behaviours of the prepared cathode materials, full cells are also assembled and tested. As shown in Fig. S14,† the electrochemical performances of the sample sintered at 775 °C also exhibits better cycling performances as well as the rate capability compared to the sample sintered at 750 °C in the full cell. The results above indicate that layered NMC71515 with the best cationic ordering and particle size can be obtained *via* balancing the surface construction and surface degradation at the optimal temperature (775 °C), which delivers the highest discharge capacity as well as excellent rate performance.

Experimental

Synthesis of NMC71515

All chemical reagents used in this study were analytical reagent grade. The precursors for NMC71515 with nominal composition of $Ni_{0.7}Mn_{0.15}Co_{0.15}(OH)_2$ were synthesized *via* a co-precipitation method. To obtain the layered oxides, the $Ni_{0.7}Mn_{0.15}Co_{0.15}(OH)_2$ was first mixed with LiOH by ball milling, then preheated at 500 °C in pure O_2 for 10 h and cooled to room temperature. The obtained intermediate was ground up, and then treated for a second time under pre-selected conditions (*i.e.*, temperature and holding time) in air to obtain the final NMC71515. To compensate for the lithium loss during high-temperature treatment, extra 5% lithium source (LiOH) was added.

Ex situ high-energy X-ray diffraction (HEXRD) measurements

High resolution XRD patterns of synthesized materials with a wavelength of 0.1867 Å were collected using Beamline XPD (28-ID-2), National Synchrotron Light Source II, Brookhaven National Laboratory. Rietveld refinements of XRD patterns were carried out using the TOPAS 3.0 software.

Materials characterization

The morphology of the prepared samples was characterized by SEM (Hitachi S4800). The surface Li_2CO_3 was measured by XPS (Thermo Fisher, ESCALAB 250X) equipped with an ion-etching system. The ion etching system used a focused monochromatic Al Kα X-ray (1486.7 eV) source for excitation and a spherical section analyzer. For comparison purposes, all of the XPS spectra were corrected based on hydrocarbon C 1s (284.6 eV). The specific surface area was obtained with the ASAP 2020 HD88 Surface Area and Porosimetry System using the Brunauer–Emmett–Teller (BET) method. Thermogravimetric analysis (TGA) was performed on a TGA/DSC1 analyzer (Mettler Toledo, Switzerland) using dry air as reaction gas. The ICP measurement was carried out with JY2000-2, HORIBA JOBINYVON.

Electrochemical measurements

A working electrode was prepared by casting a slurry of the active materials (80 wt%), Super-P carbon (10 wt%), and polyvinylidene fluoride (PVDF) binder (10 wt%) on Al foil. The graphite anode electrode was prepared by casting the slurry of the graphite (80 wt%), Super-P carbon (10 wt%) and polyvinylidene fluoride (PVDF) binder (10 wt%) on Cu foil. The areal loading for NMC71515 was approximately 0.8 mg cm^{-2}. In an argon-filled glovebox, 2032-type coin cells were assembled with metallic lithium foil (MIT Crop.) as the counter electrode and a glass fiber (Whatman, GF/D) as the separator. The discharge/charge measurements were carried out on an Arbin Instrument (BT-2400) at different rates and room temperature. The electrolyte used was 1 M $LiPF_6$ dissolved in ethylene carbonate and ethyl methyl carbonate solution (EC : EMC = 1 : 1, volume) (BASF, USA).

Conclusions

In this work, we have systematically explored the ideal synthesis conditions (*i.e.* sintering temperature and sintering time) for NMC71515. Using HEXRD, both structural ordering and disordering processes were quantitatively tracked, and the corresponding E_a values were estimated *via* the Arrhenius equation, which revealed strong correlations between Li/Ni ordering and sintering conditions. By reaching an equilibrium point (t_o) where the two processes have the same reaction rate, a structure with the highest degree of structural ordering could be obtained. Afterwards, the disordering reaction will start to take over. Additional characterizations (*e.g.* TGA and XPS) further revealed an intrinsic correlation between the Li/Ni ordering and the surface reconstruction, which involves Li_2CO_3 decomposition as well as Li loss at the particle surface. Through adequately tuning the sintering conditions in an ideal range (775–850 °C), Li-deficient phases can be avoided, and hence highly ordered NMC71515 cathode material with optimized electrochemical performances can be obtained. The concept reported in this work will provide helpful guides to the synthesis of high-performance Ni-rich layered oxide materials.

Conflicts of interest

There are no conflicts to declare.

Acknowledgements

This work was supported by the U.S. Department of Energy (DOE) Office of Energy Efficiency and Renewable Energy, Vehicle Technologies Office, Contract No. DE-SC0012704, the National Key R&D Program of China (2016YFB0700600), and the Shenzhen Science and Technology Research Grants (JCYJ20150729111733470, JCYJ20151015162256516). This research used the 28-ID-2 (XPD) beamlines of the National Synchrotron Light Source II and SEM at the Center for Functional Nanomaterials, U.S. DOE Office of Science User Facilities operated for the DOE Office of Science by Brookhaven National Laboratory under Contract No. DE-SC0012704.

Notes and references

1 J. B. Goodenough and Y. Kim, *Chem. Mater.*, 2010, **22**, 587–603.
2 J. Lu, Z. Chen and Z. Ma, *Nat. Nanotechnol.*, 2016, **11**, 1031–1038.
3 J.-M. Tarascon and M. Armand, *Nature*, 2001, **414**, 359–367.
4 J. N. Reimers and J. R. Dahn, *J. Electrochem. Soc.*, 1992, **139**, 2091–2097.
5 Z. Xiao, J. Meng, Q. Li, X. Wang, M. Huang, Z. Liu, C. Han and L. Mai, *Sci. Bull.*, 2018, **63**, 46–53.
6 L. Wang, Z. Hu, K. Zhao, Y. Luo, Q. Wei, C. Tang, P. Hu, W. Ren and L. Mai, *Sci. China Mater.*, 2016, **59**, 95–103.
7 A. R. Armstrong and P. G. Bruce, *Nature*, 1996, **381**, 499–500.
8 A. K. Padhi, K. S. Nanjundaswamy and J. B. Goodenough, *J. Electrochem. Soc.*, 1997, **144**, 1188–1194.
9 N. Yabuuchi and T. Ohzuku, *J. Power Sources*, 2003, **119–121**, 171–174.
10 Y. Xiao, T. Liu, J. Liu, L. He, J. Chen, J. Zhang, P. Luo, H. Lu, R. Wang, W. Zhu, *et al.*, *Nano Energy*, 2018, **49**, 77–85.
11 Y. Hinuma, Y. S. Meng, K. Kang and G. Ceder, *Chem. Mater.*, 2007, **19**, 1790–1800.
12 M. Broussely, P. Biensan and B. Simon, *Electrochim. Acta*, 1999, **45**, 3–22.
13 J. Kim and K. Amine, *Electrochem. Commun.*, 2001, **3**, 52–55.
14 H. Arai, S. Okada, Y. Sakurai and J. Yamaki, *J. Electrochem. Soc.*, 1997, **144**, 3117–3125.
15 H. Arai, S. Okada, Y. Sakurai and J. Yamaki, *Solid State Ionics*, 1997, **95**, 275–282.
16 H. Arai, S. Okada, H. Ohtsuka, M. Ichimura and J. Yamaki, *Solid State Ionics*, 1995, **80**, 261–269.
17 F. Wu, J. Tian, Y. Su, J. Wang, C. Zhang, L. Bao, T. He, J. Li and S. Chen, *ACS Appl. Mater. Interfaces*, 2015, **7**, 7702–7708.
18 X.-J. Wang, H.-Y. Chen, X. Yu, L. Wu, K.-W. Nam, J. Bai, H. Li, X. Huang and X.-Q. Yang, *Chem. Commun.*, 2011, **47**, 7170.
19 G. L. Xu, Z. Chen, G. M. Zhong, Y. Liu, Y. Yang, T. Ma, Y. Ren, X. Zuo, X. H. Wu, X. Zhang, *et al.*, *Nano Lett.*, 2016, **16**, 3955–3965.
20 X. Yu, H. Pan, W. Wan, C. Ma, J. Bai, Q. Meng, S. N. Ehrlich, Y. S. Hu and X. Q. Yang, *Nano Lett.*, 2013, **13**, 4721–4727.
21 K.-W. Nam, S.-M. Bak, E. Hu, X. Yu, Y. Zhou, X. Wang, L. Wu, Y. Zhu, K.-Y. Chung and X.-Q. Yang, *Adv. Funct. Mater.*, 2013, **23**, 1047–1063.
22 F. Wang, L. Wu, B. Key, X. Q. Yang, C. P. Grey, Y. Zhu and J. Graetz, *Adv. Energy Mater.*, 2013, **3**, 1324–1331.
23 J. Zhao, W. Zhang, A. Huq, S. T. Misture, B. Zhang, S. Guo, L. Wu, Y. Zhu, Z. Chen, K. Amine, *et al.*, *Adv. Energy Mater.*, 2017, **7**, 1–13.
24 D. Wang, R. Kou, Y. Ren, C. J. Sun, H. Zhao, M. J. Zhang, Y. Li, A. Huq, J. Y. P. Ko, F. Pan, *et al.*, *Adv. Mater.*, 2017, **29**, 1–8.
25 M.-J. Zhang, G. Teng, Y. K. Chen-Wiegart, Y. Duan, J. Y. P. Ko, J. Zheng, J. Thieme, E. Dooryhee, Z. Chen, J. Bai, *et al.*, *J. Am. Chem. Soc.*, 2018, **140**, 12484–12492.
26 Y. Duan, B. Zhang, J. Zheng, J. Hu, J. Wen, D. J. Miller, P. Yan, T. Liu, H. Guo, W. Li, *et al.*, *Nano Lett.*, 2017, **17**, 6018–6026.
27 K. Matsumoto, R. Kuzuo, K. Takeya and A. Yamanaka, *J. Power Sources*, 1999, **81–82**, 558–561.
28 J. Zheng, Y. Hou, Y. Duan, X. Song, Y. Wei, T. Liu, J. Hu, H. Guo, Z. Zhuo, L. Liu, *et al.*, *Nano Lett.*, 2015, **15**, 6102–6109.
29 N. Mahne, S. E. Renfrew, B. D. Mccloskey and S. A. Freunberger, *Angew. Chem., Int. Ed.*, 2018, 5529–5533.
30 S. E. Renfrew and B. D. McCloskey, *J. Am. Chem. Soc.*, 2017, **139**, 17853–17860.
31 N. Mijung, Y. Lee and J. Cho, *J. Electrochem. Soc.*, 2006, **153**, A935.
32 E. Antolini, *Phys. Status Solidi A*, 1999, **173**, 357–364.
33 E. Antolini, *J. Mater. Chem.*, 1998, **8**, 2783–2786.
34 E. McCalla, G. H. Carey and J. R. Dahn, *Solid State Ionics*, 2012, **219**, 11–19.
35 T. Ohzuku and Y. Makimura, *Chem. Lett.*, 2001, **2**, 744–745.
36 D. Wang, R. Kou, Y. Ren, C. J. Sun, H. Zhao, M. J. Zhang, Y. Li, A. Huq, J. Y. P. Ko, F. Pan, *et al.*, *Adv. Mater.*, 2017, **29**, 1–8.
37 H. Liu, Y. Yang and J. Zhang, *J. Power Sources*, 2007, **173**, 556–561.
38 L. Xin, Y. Liu, B. Li, X. Zhou, H. Shen, W. Zhao and C. Liang, *Sci. Rep.*, 2014, **4**, 1–7.